Thermal Effect on the Performance of an AC-DBD Plasma Actuator

Lu Shen *
Nanyang Technological University, Singapore

Zongnan Chen † and Chih Yung Wen‡
The Hong Kong Polytechnic University, Hong Kong, PRC

The dielectric barrier discharge (DBD) plasma actuator is a popular technology for active flow control; however, the influence of the heat generated by the actuator on its performance is seldom mentioned. In this work, an experimental investigation is conducted to evaluate the interaction between spontaneous heat generation and the performance of an AC-DBD plasma actuator. The characteristics of the AC-DBD plasma actuator are examined temporally in quiescent air, including the profile of the induced flow, capacitance properties, power consumption, plasma light emission, and surface temperature. The particle image velocimetry shows that the velocity profile of the induced flow increases temporally, indicating enhanced momentum injection by the AC-DBD plasma actuator. The capacitance, power consumption, plasma brightness and surface temperature increase with the operation time analogously to exponential curves ($f(x) = a - b\exp^{-cx}$). And values of these properties are proportional to 3.5 power of the applied voltage. The dielectric surface is categorized into three typical streamwise regions according to the heat generation characteristics: the plasma region, the insulated electrode region, and the far field region. The dominant heat generation occurs in the plasma region due to the plasma discharge. The temperature increase of the local dielectric and the gas-plasma mixture enlarges the actuator capacitance, benefits the local induced electric field, and results in longer mean free paths of particles and stronger discharges accordingly. Thus, the spontaneous heat generation affects the induced ionic wind, and the performance of the AC-DBD plasma actuator is time dependent during the early period of the operation.

Nomenclature

C = capacitance, C

C_a = air capacitance, C

*Research Fellow, School of Mechanical and Aerospace Engineering, shenlu@ntu.edu.sg.
†Ph.D student, Department of Mechanical Engineering.
‡Professor, Department of Mechanical Engineering, cywen@polyu.edu.hk, AIAA associate fellow.

C_{cold} = non-ionization capacitance, C

C_d = dielectric capacitance, C

C_{eff} = effective capacitance, C

E = electric field, V/m

f = frequency, Hz

l = length, mm

P_D = dielectric heating power, W

P_E = electrical power, W

P_M = mechanical power, W

Q = electric charge, C

$\dot{q}$ = heating power, W

R = resistance, Ω

T = temperature, ^oC

t = time, s

u = velocity, m/s

V_a = voltage across air, kV

V_C = voltage across the capacitor, kV

V_{DBD} = instant applied voltage, kV

V_d = voltage across the dielectric layer, kV

V_{pp} = peak-to-peak voltage, kV

V_R = voltage across the resistance, kV

x, y, z = coordinate, mm

$tan\delta$ = dielectric loss tangent

ρ = density

I. Introduction

THE dielectric barrier discharge (DBD) plasma actuator has become an attractive pneumatic technique for active flow control in the past decade. It has been widely applied to separation control [1–3], boundary layer control [4, 5], velocity fluctuation control [6, 7], noise control [8, 9], and maneuvering control [10–12]. A typical DBD plasma actuator consists of four parts: an exposed electrode, an insulated electrode, a dielectric layer sandwiched between two electrodes, and a high-voltage and high-frequency power supply. In many studies, plasma actuators are driven by alternating current (AC), known as AC-DBD actuators. The details of AC plasma actuation can be found in the

references [3, 11, 13]. Once the AC-DBD plasma actuator is ignited, the neutral air near the exposed electrode is ionized to form plasma. Due to the electric field between two electrodes, the ions move from one electrode to another and collide with the neutral gas molecules. Thus, a local flow motion is induced, the so-called ionic wind [14]. The characteristics of dielectric barrier discharge were reviewed in detail by Brandemburg [15], and applications of AC-DBD plasma actuators in aeronautic engineering were well reviewed by Moreau [16] and Corke, *et al*. [17].

In most applications, the AC-DBD plasma actuator is used as a zero-net-mass-flux actuator to inject the momentum into the flow field [18]. It is also commonly referred to as a nonthermal plasma actuator, as the gas temperature is close to the ambient temperature while the electron energy is in the order of 10 eV [19]. However, experimental measurements [20] showed that the electromechanical efficiency of the AC-DBD plasma actuator is rather low. Most of the energy from the actuator is released as thermal energy to the surrounding air and to the actuator itself [13, 21]. Joussot, *et al*. [22] and Tirumala, *et al*. [23] measured the surface temperature of the AC-DBD plasma actuator in quiescent air with infrared cameras and found that the surface temperature increased significantly. Rodrigues, *et al*. [24] developed an air flow calorimetric technique to measure the heat release of the AC-DBD plasma actuator. They found that the heat generation efficiency is dependent on the thickness of the dielectric layer. The heat generation phenomenon was also observed with Schlieren measurements in the micro-, milli-, and nano-second DBD cases [25–27]. The heat generation of the AC-DBD plasma actuator has also been experimentally applied for de-icing and anti-icing [28–31]. The performance of an AC-DBD plasma actuator is determined by many factors, such as the geometry, applied voltage, operation mode, and ambient pressure [32–35]. It has also been noted that the temperature of the ambient air [36] and the temperature of the dielectric layer [37] affect the induced velocity field. Versailles, *et al*. [36] suggested that the mean free path of gas molecules increases when the ambient temperature is high. Thus, ions can obtain more kinetic energy from the electric field before they collide with neutral gas molecules, leading to enhanced global momentum transfer.

Due to rather limited studies on the spontaneous thermal effect on the performance of the AC-DBD plasma actuator, it is necessary to further investigate the interaction between the induced flow and the spontaneous heat generation for applications of AC-DBD plasma actuators to active flow control. The primary objective of the present study is to evaluate the performance of an AC-DBD plasma actuator temporally through an experimental investigation. The induced flow field, actuator capacitance, power consumption, plasma emission, and surface temperature of the dielectric layer were measured temporally, and an analysis was conducted to explain the influence on the induced flow due to the heat generated by the AC-DBD plasma actuator.

II. Experiment Setup

The circuit of the AC-DBD plasma actuator used in this study is illustrated in Fig. 1. Electrodes of the actuator were made of copper film with a thickness of 0.025 *mm*. The effective length of the actuator was 100 *mm*. The widths of the

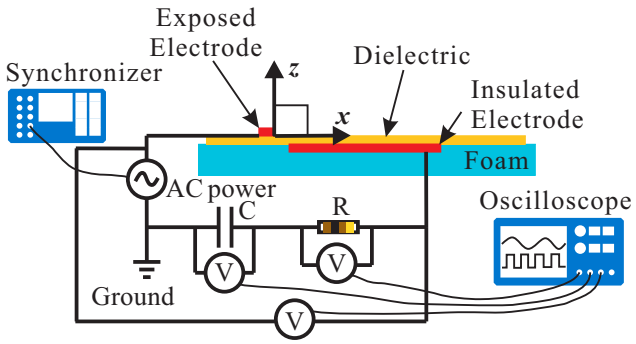

Fig. 1 Schematics of the electric circuit of the AC-DBD plasma actuator.

exposed electrode and the insulated electrode were 2 *mm* and 20 *mm*, respectively. There was a 2 *mm* gap between the electrodes. The dielectric layer was made of acrylic plate (150 *mm* × 200 *mm*) with a thickness of 2 *mm*. The lower surface of the insulated electrode was covered with two layers of 0.06 μm thick Kapton film to isolate it from the air. A resistance $R = 100$ *ohm* and a Class I ceramic capacitor $C_c = 33\ nF$ were connected in series on the grounded side to measure the power consumption of the circuit[38]. The applied voltage (V_{DBD}), the voltage across the resistance (V_R) and the voltage across the capacitor (V_C) were measured simultaneously using an oscilloscope (Keysight DSOX2014A) with voltage probes (Teckronix P6015A and Agilent N2862B). The AC power supply was in a sinusoidal waveform with a frequency around 20 *kHz*. A synchronizer (BNC 575) was used to trigger the power supply and it was also connected to other diagnostic devices. It should be noted that the diagnosis data in different individual cases were examined. $t = 0$ was defined as the moment that the AC-DBD plasma actuator was turned on. The applied peak-to-peak voltage varied from $V_{pp} = 12\ kV$ to $V_{pp} = 18\ kV$.

The experiment was conducted in the test section of a closed-loop wind tunnel in the Hong Kong Polytechnic University, to ensure a quiescence environment for the AC-DBD plasma actuator. The flow was generated only due to the AC-DBD plasma actuator and no external flow was applied. The size of the test section was 600 *mm* × 600 *mm* × 1200 *mm*. The AC-DBD plasma actuator was placed on a thick foam plate to insulate the heat transfer from the bottom surface. To avoid any light reflection during the experiment, the upper surface of the actuator (except for the exposed electrode) was painted in flat black. During the experiment, the room temperature of the laboratory remained nearly constant by a central air-conditioning system. A temperature probe was used to measure the air temperature in the wind tunnel. The air temperature change was less than 1°C. After each test, the wall of the test section was removed to initialize the ambient condition. All the diagnostics were conducted at least twice, and comparisons of results showed that observations were repeatable.

The power consumption of the AC-DBD plasma actuator was calculated using the measurements from the oscilloscope. For each instant, the sampling duration was $200\times10^{-6}\ s$, in which 3 completed cycles of the sinusoidal wave could be included. The resolution was $4\times10^{-9}\ s$. The time interval between sampling instants was 2 *s*, corresponding to

a sampling frequency of 0.5 Hz. The measurement uncertainties were 200 $Volt$ for $V_{DBD}(t)$ ($\sim$ 1.1% of V_{pp}), and 0.03 $Volt$ for $V_C(t)$ ($\sim$ 1.3% of the peak value). For the in-line monitor capacitor, the change in capacitance with voltage is negligible[39]. The electric discharge Q in the circuit were calculated using the voltage across the capacitor, $dQ = dV_C \times C_c$. Then, the powers per unit length were defined as

$$P_E = \frac{1}{\tau l} \oint Q(t)\, dV_{DBD} \tag{1}$$

where $\tau = 50 \times 10^{-6} s$ is the period of one sinusoidal cycle, and $l = 0.1\ m$ is the length of the AC-DBD plasma actuator.

The surface temperature of the AC-DBD plasma actuator was measured using an infrared camera (FLIR A6751sc) with a 25 mm lens. The calibrated temperature ranged from 10°C to 90°C and the measurement accuracy was ±2 °C. In this paper, the change in temperature (ΔT=T_t-$T_{initial}$) is presented rather than the absolute temperature. The initial temperature $T_{initial}$ of the dielectric layer was measured before each experiment. The sampling frequency of the infrared camera was set at 1.7 Hz with a frame resolution of 5.8 pixels/mm. In addition, another digital camera (Nikon D750 with a 180 mm macro lens) was used to visualize the plasma generated by the AC-DBD plasma actuator. The exposure time was set at 1/10 s and the ISO was fixed at 6400. The time interval between frames was around 5 s. The frame resolution was 112 pixels/mm.

Two-dimensional particle image velocimetry (PIV) measurement was conducted to obtain the details of the AC-DBD induced flow field. A dual-pulse laser (EverGreen 532 nm, with each pulse of 600 mJ) was used to light up the flow field in the x-z plane (see Figure 1). The frames were captured using a CCD camera (HiSense 4M) with a resolution of 2048 × 2048 pixels. The entire tunnel was uniformly seeded with oil particles (normal diameter 1 μm) from an aerosol generator (TSI 9307-6) [40]. The analysis was conducted using DynamicStudio software with adaptive PIV correlation. The initial interrogation area was 32 × 16 pixels. The measurement uncertainty of the particle displacement was about 0.05 pixels [41]. Thus, the corresponding uncertainty of the velocity was less than 0.02 m/s.

III. Results and Discussion

A. Plasma light emission

Although the lifetime of the plasma discharge is very short, the high frequency AC-DBD plasma actuator reignites the old plasma discharges at the same position in every AC period due to the memory phenomenon [42]. Thus, a long exposure (compared to the plasma discharge duration) digital camera could obtain a time-averaged distribution of the plasma discharges, which highlights dominant features during this period. Figure 2(a) shows three typical examples of plasma discharges after running the actuator with $V_{pp} = 18\ kV$ for $t = 16\ s$, $t = 102\ s$, and $t = 204\ s$, respectively. At each instant, three typical plasma structures are observed: the small discharge spots, the streamers and the glow region. Overall, the discharging is not isotropic along the electrodes. However, the distribution of aforementioned

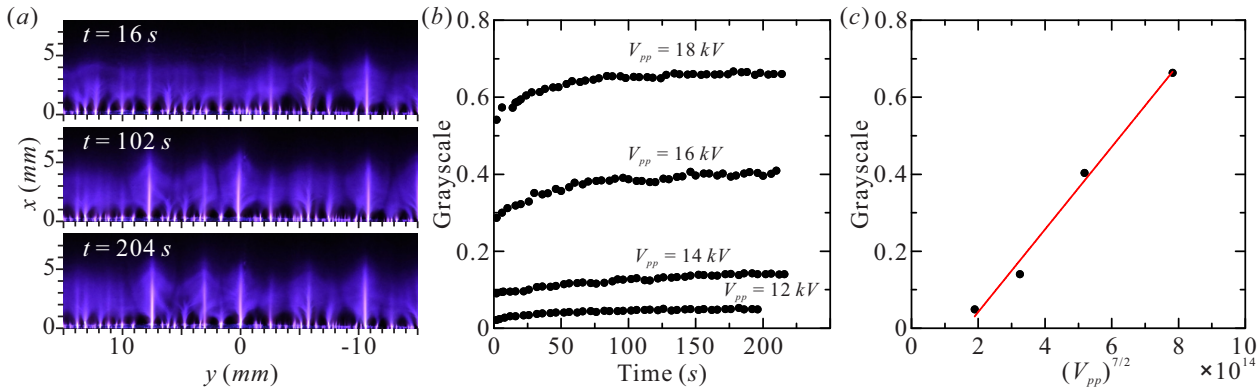

Fig. 2 (a) Frames of the plasma generated by the AC-DBD plasma actuator with V_{pp} = 18 kV at t = 16 s, t = 102 s and t = 204 s, respectively; (b) the spanwise-averaged temporal brightness of plasma at x = 3 mm with different V_{pp}; and (c) the gray-scale brightness of plasma at t = 196 s versus $(V_{pp})^{3.5}$ with a linear fitting line.

structures is quasi uniform. The small discharge spots are very close to the exposed electrode, and they only exist in the region $x < 1$ mm. At some positions, the discharge spots are replaced by strong streamers with some weak branching streamers. Surrounding these plasma streamers, there are glow regions. Since frames were taken with long exposure durations, some unsteady branching streamers may appear as the glow in these frames. A comparison among these frames indicates that both the length and the brightness of the streamers are developing with the active duration. At t = 16 s, the length of the streamers is less than 4 mm; while at t = 204 s, it is close to 5 mm. At the same time, the area of the glow regions is enlarging.

To further illustrate the unsteady plasma developing process, the spanwise-averaged plasma emission brightness for each instance was obtained by averaging the brightness in the line at x = 3 mm. These spanwise-averaged results were then plotted in the time sequence to demonstrate the temporal evolution of the plasma emission brightness, as shown in Fig. 2(b). For each applied V_{pp}, the overall evolution of the plasma brightness was analogous to the exponential function $f(x) = a - b\exp(-cx)$. This result indicates that the AC-DBD plasma actuator was unsteady in the beginning and it became quasi steady after a long period of operation. In the case with a higher V_{pp}, the temporal difference of the plasma brightness was much larger. Another notable tendency showing in Fig. 2(b) is that the plasma brightness increases significantly with the applied V_{pp}. The corresponding gray-scale brightness of plasma at t = 196 s in these cases are plotted in Fig. 2(c). Here, the $x-$axis is the 3.5 power of the applied peak-to-peak voltage, $(V_{pp})^{3.5}$, which is known to be proportional to the power consumption[43]. As observed in Fig. 2(c), the plasma brightness increases linearly with $(V_{pp})^{3.5}$. Therefore, the plasma brightness is proportional to the power consumption.

B. Capacitance variation and power consumption

Figure 3(a) shows a typical example of instant Q-V cyclograms (Lissajous figures) of the AC-DBD plasma actuator with V_{pp} = 18 kV, which includes important details to estimate the electric performance of the actuator[43]. It is

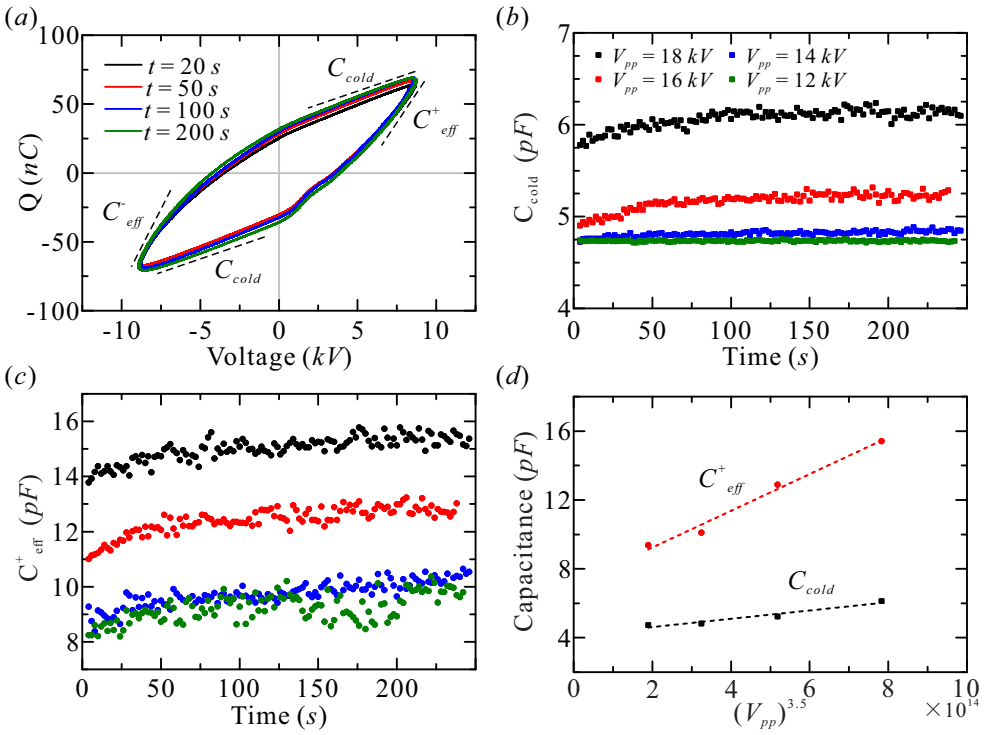

Fig. 3 (a) The electric charge Q through the circuit versus the applied voltage with V_{pp} = 18 kV (Lissajous figures); (b) the time histories of cold (non-ionization) capacitance C_{cold} of the AC-DBD plasma actuator with different V_{pp}; (c) the time histories of effective capacitance C^{+}_{eff} of the AC-DBD plasma actuator with different V_{pp}; and (d) the capacitances at t = 200 s versus $(V_{pp})^{3.5}$ with linear fitting lines.

obvious that the electric charge Q was increasing during the operation. At $t = 20\ s$, the maximum electric charge in the circuit was $Q = 63.4\ nC$; while at $t = 200\ s$, it increased to $Q = 68.9\ nC$, corresponding to an increment of 8.7%. To better understand the temporal behavior of the AC-DBD plasma actuator, two significant capacitance values, C_{cold} for the non-ionization (cold) capacitance of the actuator, and C_{eff} for the effective ionization capacitance, are introduced (see dashed lines in Fig.3(a)). The C_{eff} can be further categorized into C^{+}_{eff} during the voltage rise half cycle (the input AC volateg signal from $-90°$ to $90°$) and C^{-}_{eff} during the voltage fall half cycle (the input AC voltage signal from $90°$ to $270°$). The local capacitance was calculated as $C(t) = dQ(t)/dV(t)$. Then the instantaneous capacitances during $1/8\tau \sim 1/4\tau$, $5/8\tau \sim 3/4\tau$, and both $3/8\tau \sim 1/2\tau$ with $7/8\tau \sim \tau$, were averaged as C^{+}_{eff}, C^{-}_{eff}, and C_{cold} in one V_{pp} cycle, respectively. This method can provide a result very close to that produced by the capacitance histogram analysis[43].

The time histories of cold (non-ionization) capacitances are plotted in Fig.3(b) for cases with different V_{pp}. It is obvious that the increase of the applied voltage enlarges the cold capacitance. With $V_{pp} = 12\ kV$, the cold capacitance is almost constant at $C_{cold} = 4\ pF$; while it dramatically increases to a mean value around $C_{cold} = 6\ pF$ with $V_{pp} = 18\ kV$. In addition, the cold capacitances rise temporally in these cases, excepting that with $V_{pp} = 12\ kV$. For instance, the capacitance change between $t = 10\ s$ and $t = 200\ s$ is $\Delta C_{cold} \approx 0.3\ pF$ (5%) with $V_{pp} = 18\ kV$. The overall evolutions of these cold capacitances are analogous to the exponential function $f(x) = a - b\exp(-cx)$. This result indicated that the electric properties of the AC-DBD plasma actuator varies temporally even during the non-ionization period. Even though the discharge type during the voltage rise half cycle is the streamer mode, while it is the glow mode during the voltage fall half cycle[14]. The different discharge modes only have a very small impact on the result of effective capacitances ($C^{-}_{eff}/C^{+}_{eff} \approx 1$) [43]. The time histories of C^{+}_{eff} are shown in Fig.3(c). Similar to those shown in Fig.3(b), the increase of the applied voltage significantly enlarges the value of effective capacitances. The increment of C^{+}_{eff} from $V_{pp} = 12\ kV$ to $V_{pp} = 18\ kV$ is even larger than 50%. For each time history of C^{+}_{eff}, it also follows an increasing tendency analogous to the exponential function $f(x) = a - b\exp(-cx)$. The increment of effective capacitance with $V_{pp} = 18\ kV$ is $\Delta C^{+}_{eff} \approx 1.4pF$ (10%) from $t = 10\ s$ to $t = 200\ s$, much higher than that for the cold capacitance. On the basis of this result, it can be expected that the discharging of the AC-DBD plasma actuator is varying during the experiment with a fixed V_{pp}, consistent to the observation of plasma light emission in Fig.2. In Fig.3(d), the capacitances at $t = 200\ s$ are plotted versus $(V_{pp})^{3.5}$. The linear fitting lines are shown as the dash lines. It is obvious that these capacitance data fit well with the linear function, indicating that the electric properties of the AC-DBD plasma actuator is also related with the power consumption.

Figure 4(a) shows temporal evolutions of the actuator power consumption with various V_{pp}, obtained using Eq.1 based on the capacitor method. For instance, in the case of $V_{pp} = 18\ kV$, the power consumption per spanwise length is about $P_E \approx 65\ W/m$ at the beginning; it then increases exponentially to $P_E \approx 72\ W/m$ at $t = 200\ s$. Similar increase tendencies of the power consumption are also noted in the other cases. Thus, it can be known that the electric

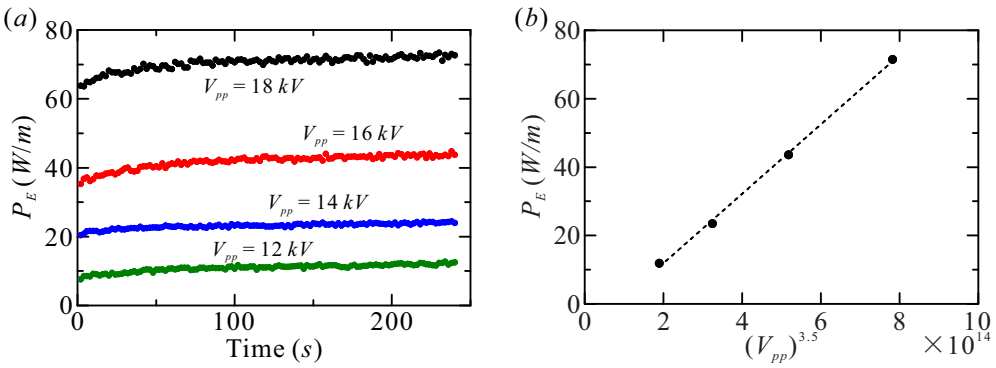

Fig. 4 (a) The time histories of the power consumption of the AC-DBD plasma actuator with different V_{pp}; and (b) the power consumption at $t = 200\ s$ versus $(V_{pp})^{3.5}$ with a linear fitting line.

performance of the AC-DBD plasma actuator is time-dependent and it varies a lot at the early time of the operation. In other word, the electric performance of the AC-DBD plasma actuators needs a period of operation time to be quasi steady. It is also obvious in Fig.4(a) that the power consumption increases greatly with the increase of applied V_{pp}. For comparison, the power consumptions at $t = 200\ s$ in these case are plotted versus $(V_{pp})^{3.5}$ in Fig.4(b). As highlighted by the linear fitting line, the power consumption of the actuator is almost proportional to $(V_{pp})^{3.5}$, which is consistent with previous studies[32, 43].

Following Jukes, *et al.* [44] and Kroschwitz [45], the electric power consumption per length due to the dielectric heating effect, P_D, can be calculated as

$$P_D = 2\pi \frac{1}{l} f V_{pp}^2 C tan\delta \tag{2}$$

where f is the frequency of the applied voltage, $C = 0.5(C_{cold} + C_{eff})$ is the capacitance of the actuator, and $tan\delta$ is the dielectric loss tangent. In this study, the dielectric loss tangent is $tan\delta = 0.0014$ with frequency $f = 20\ kHz$ at $T_\infty = 30$ °C and this parameter of acrylic is insensitive to temperature.[46] The results of P_D at different V_{pp} and the corresponding ratios of P_D/P_E are shown in Table 1. For $V_{pp} = 12\ kV$, the dielectric heating can approach 18.3% of the total electric power consumption at the beginning. Then it reduces to 14.8% at $t = 200\ s$. Nevertheless, at a higher peak-to-peak voltage, the percentage of the dielectric heating in the total electric power consumption is less, for instance, P_D/P_E is only 8.8% for $V_{pp} = 18\ kV$. This makes sense because the total electric power consumption is proportional to the peak-to-peak voltage with a power of 3.5, $P_E \sim (V_{pp})^{3.5}$; while the dielectric heating is proportional to the peak-to-peak voltage with a power of 2, $P_D \sim (V_{pp})^2$. Overall, the dielectric heating power makes only a small contribution to the heat generation of the actuator.

C. Induced flow

The PIV measurement was conducted in the x-z plane, locating at the middle of the actuator. The data acquisition duration was 200 seconds. In Fig.5, the time-averaged velocity contours with the velocity vectors in the case of

Table 1 The power consumption due to the dielectric heating.

$V_{pp}(kV)$	P_D at $t = 4s(W/m)$	P_D/P_E (%)	P_D at $t = 200s(W/m)$	P_D/P_E (%)
12	1.6	18.3	1.7	14.8
14	2.2	10.4	2.5	10.6
16	3.6	9.8	4.2	9.7
18	5.5	8.8	6.3	8.7

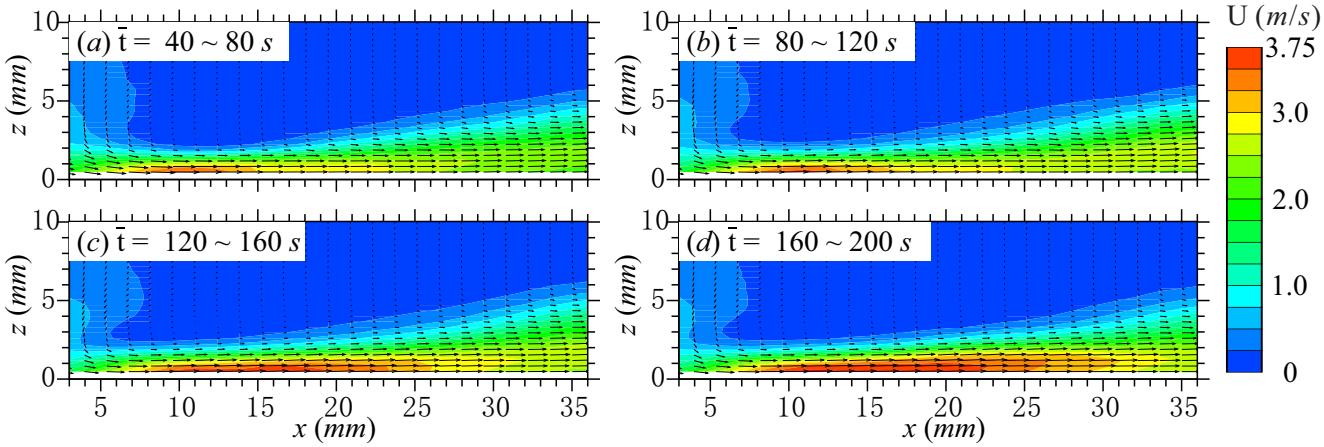

Fig. 5 The velocity contours of the time-averaged PIV results in the *x*-*z* plane with the superimposed velocity vectors.($V_{pp} = 18\ kV$)

$V_{pp} = 18\ kV$ are demonstrated from $t = 40\ s$ to $t = 200\ s$, with an average time step of 40 seconds. In all of the frames, the AC-DBD plasma actuator generates a wall-jet-like ionic wind on the surface. As the working time increases, the observed velocity magnitude of the induced flow increases gently. At the same time, the region with the large velocity magnitude is obviously stretched downstream, and the position where the highest velocity occurs also moves downstream. However, the time-averaged thickness of the induced flow changes little. In this measurement, the maximum time-averaged velocity reaches 3.75 m/s in $160 \sim 200\ s$, while the instantaneous velocity map at $t = 200\ s$ shows that the maximum instantaneous velocity can even exceed 4 m/s.

Figure 6 shows the temporal development of $\sum_{z=0}^{z=10} (u_z)^2$ at the location of $x = 20.3\ mm$ with different applied voltages. As can be seen in Fig.6, the instant value of $\sum (u_z)^2$ was oscillating greatly, especially in cases with higher V_{pp}, indicating that the induced ionic wind was unsteady and the mechanical power output of the actuator varied temporally. This temporal velocity oscillation of the ionic wind can be attributed to the less homogeneous discharge with the higher applied voltage[14] and the stronger three-dimensional effect in the downstream flow field due to the filament discharge[47]. Even though, the sum of $(u_z)^2$ still can be roughly proportional to the momentum ($\rho \int U_z^2\ dz$) of the local ionic wind. Linear fitting was applied on these experimental data and the corresponding fitting lines are shown in Fig.6. Notably, the linear fitting lines are intended to illustrate the general trends in time. No quantitative interpretation from the linear fitting will be made in the discussion. It is obvious that these fitting lines have positive slopes, showing

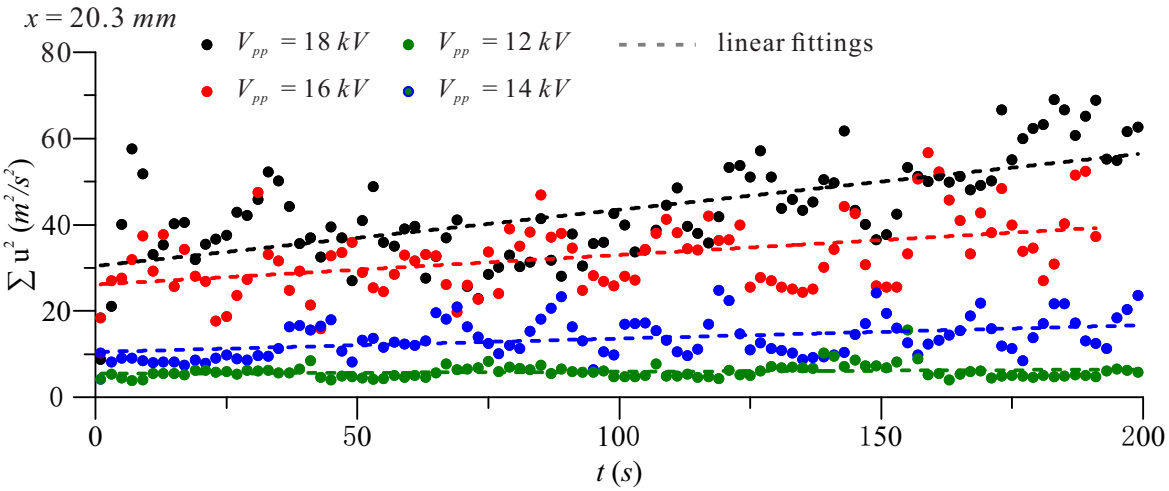

Fig. 6 The development of $\sum_{z=0}^{z=10} (u_z)^2$ at $x = 20.3\ mm$ and $y = 0$ in cases with different applied voltages; each data point is a time average value of 2 seconds for a single test and experimental data are fitted by linear functions.

the temporally increase of the mean $\sum (u_z)^2$. For the case of $V_{pp} = 18\ kV$, the fitting line slope is 0.13 m^2/s^3, which is quite large; the time-averaged $\sum (u_z)^2$ increased from 38.3 m^2/s^2 during $t = 0 \sim 50\ s$ to 56.0 m^2/s^2 during $t = 150 \sim 200\ s$, corresponding to an increment of 46.4 %. The other cases also show the similar tendency of $\sum (u_z)^2$ during the experiment. However, the changes became smaller when the applied voltage was reduced. For instance, the time-averaged $\sum (u_z)^2$ changed from 5.4 m^2/s^2 over $t = 0 \sim 50\ s$ to 6.0 m^2/s^2 over $t = 150 \sim 200\ s$ in the case of $V_{pp} = 12\ kV$, corresponding to an increment of only 10.4 %. Therefore, it can be concluded that the mechanical power output of the actuator is enhanced with the increasing of the actuator activation time. The aerodynamic performance of the AC-DBD plasma actuator is time dependent during the early period of the operation.

D. Dielectric temperature

Examples of temperature changes ΔT on the dielectric surface at times $t = 16\ s$, $t = 102\ s$ and $t = 204\ s$ in the cases of $V_{pp} = 14\ kV$ and $V_{pp} = 18\ kV$ are presented in Fig.7(a) and Fig.7(b), respectively. In both cases, the contours of the temperature increment near the exposed electrode are not homogeneous in the spanwise direction. There are highly concentrated temperature change distributions near the edge of the exposed electrode, which represent the highest temperature rises on the dielectric surface. These regions correspond to the small discharge spots and the streamers in Fig.2(a). The high temperature increment is a result of the very low but high-frequency heating of the plasma discharge [42]. As shown in Fig.7(a), the maximum temperature increment on the dielectric at $t = 16\ s$ is around $\Delta T = 20\ ^\circ C$; at $t = 102\ s$, it increased to $\Delta T \approx 30\ ^\circ C$; and at $t = 204\ s$, the maximum temperature increment changes little, while the area of high temperature regions increases greatly, which is clearly shown by the moving contour lines. This expansion of high temperature regions near the exposed electrode can be a result of the aforementioned expanding

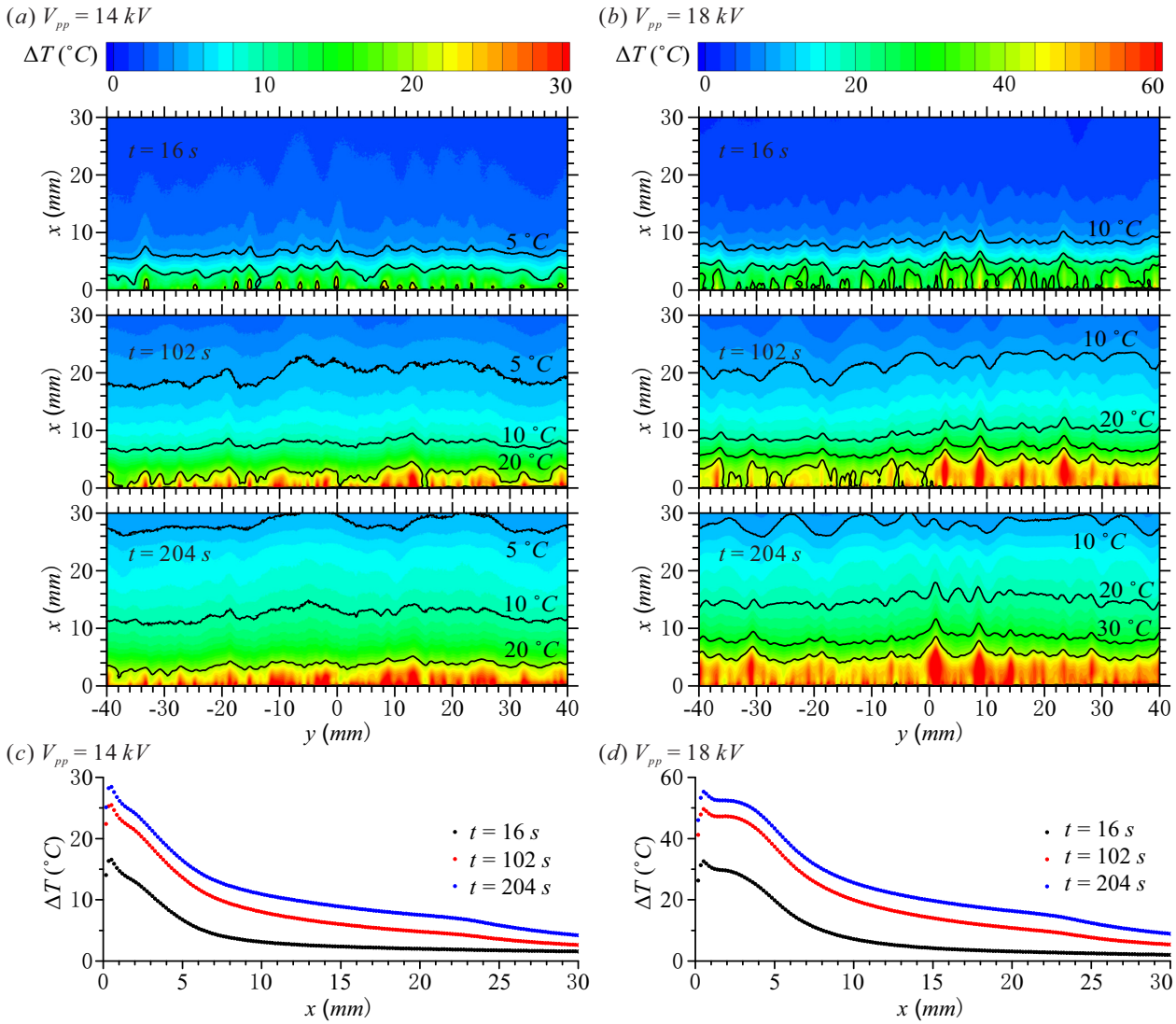

Fig. 7 Instantaneous temperature change distributions of the AC-DBD plasma actuator with (a) V_{pp} = 14 kV and (b) V_{pp} = 18 kV at t = 16 s, t = 102 s and t = 204 s, respectively; (c) and (d) corresponding spanwise-averaged (y = −40 to 40 mm) temperature change distributions along x−axis.

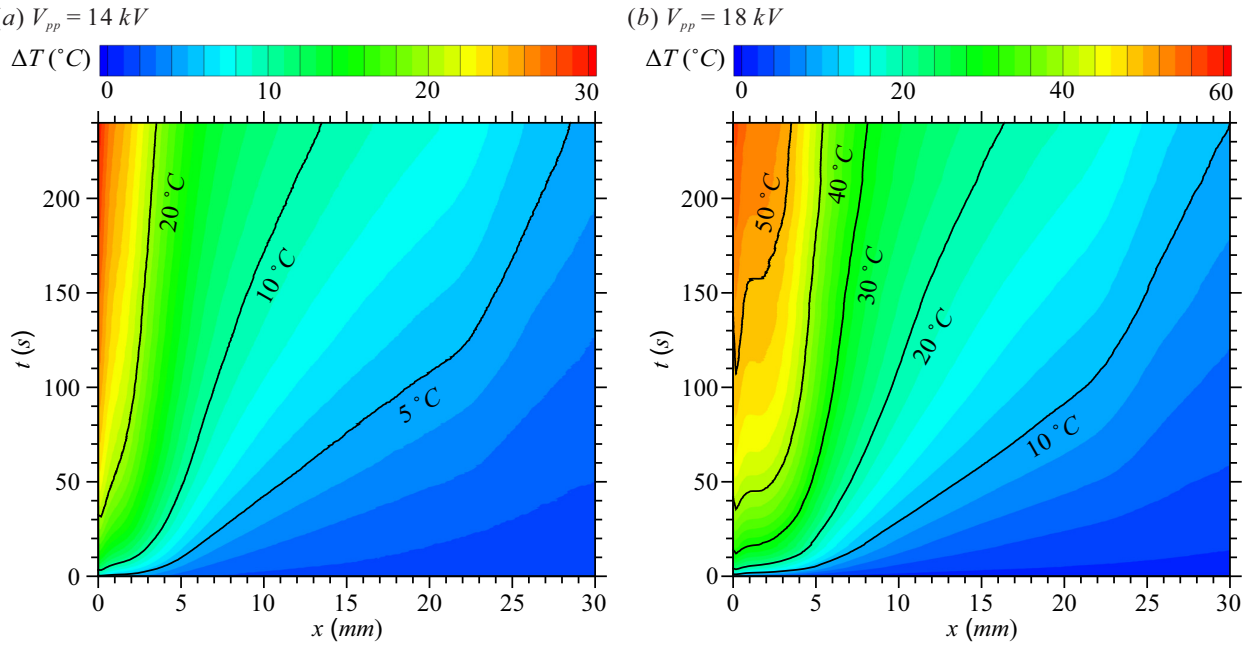

Fig. 8 The spanwise-averaged ($y = -40$ to 40 mm) spatiotemporal temperature distribution of the AC-DBD plasma actuator with (a) $V_{pp} = 14$ kV and (b) $V_{pp} = 18$ kV.

plasma structures (see in Fig.2(a)). Meanwhile, in the downstream region, the nonuniformity of temperature increment becomes less in the spanwise direction. The same evolution of the temperature increment on the dielectric layer can also be seen in Fig.7(b) with a higher V_{pp}.

To understand the evolution of temperature changes in the streamwise direction, the spanwise-averaged ($y = -40$ to 40 mm) temperature change is plotted, as shown in Fig.7(c) and Fig.7(d) for $V_{pp} = 14$ kV and $V_{pp} = 18$ kV, respectively. Because of the averaging, the spanwise-averaged temperature increment is smaller than the highest temperature. However, the spanwise average is still useful for demonstrating the temperature changes on the dielectric surface. At each instant, the temperature increment near the exposed electrode is much higher than that in the downstream region, and the maximum temperature increment occurs near the location $x = 0.5$ mm due to the uniform discharge spots near the exposed electrode. In the area of $x = 0.5 \sim 1$ mm, there is a small temperature drop, because of the absence of the plasma spots, as shown in Fig.2. Benefiting from the uniformly distributed glow regions and the plasma streamers, the temperature increment at $t = 204$ s doesn't change much until it is near $x = 2$ mm in Fig.7(c) and $x = 3$ mm in Fig.7(d). After these two points, the temperature increment begins to decrease significantly as the position comes close to the edge of the plasma region (see in Fig.2(a)). Later, the temperature increment decreases gradually as the y distance increases. It is worthy to note that the temperature increment decreases slightly faster after $x = 22$ mm in both cases.

The spatiotemporal variations of the spanwise-averaged temperature with $V_{pp} = 14$ kV and $V_{pp} = 18$ kV are plotted in Fig.8 as contour fields. The horizontal axis is the x distance and the vertical axis is the time. Near the exposed electrode, significant temperature rises are observed during the early decades seconds. In Fig.8(a), the temperature

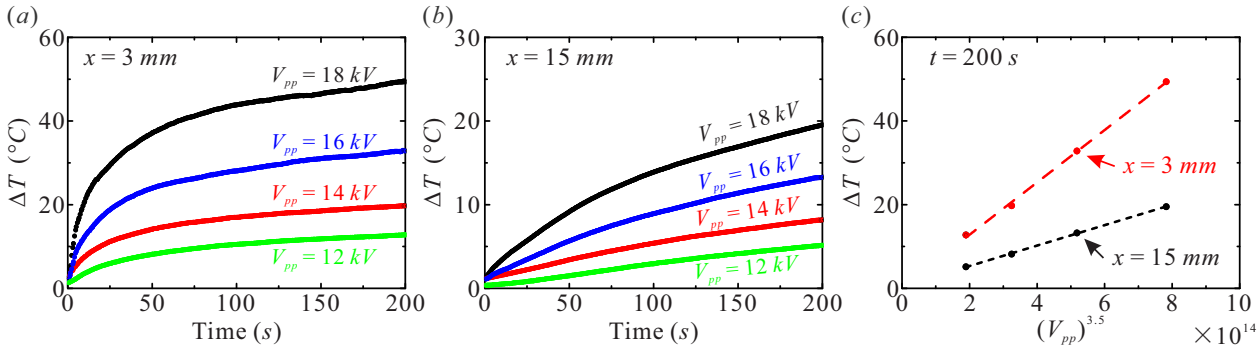

Fig. 9 Spanwise-averaged ($y = -40$ to 40 mm) temporal temperature increment ΔT at (a) $x = 3$ mm and (b) $x = 15$ mm with different V_{pp}; and (c) the temperature at $x = 3$ mm and $x = 15$ mm after $t = 200$ s versus $(V_{pp})^{3.5}$ with linear fitting lines.

increment has reached $\Delta T = 20$ ° at $t = 30$ s; and in Fig.8(b), it only takes several seconds to approach $\Delta T = 20$ °. After these rapid increase periods, although the temperatures continue to increase, the temperature growth rates become smaller. In the downstream region, the temperature increment is much slower, which is also clearly seen in Fig.7(c) and Fig.7(d). Meanwhile, the time differences between two adjacent counter lines show the tendency that the temperature growth rate in the downstream region is also decreasing temporally. In both Fig.8(a) and Fig.8(b), there are two main abrupt changes during the development of the spatiotemporal temperature distribution, indicating by the counter lines. With $V_{pp} = 14$ kV, the first turn occurs near $x = 4$ mm at $t = 5$ s; in the case of $V_{pp} = 18$ kV, it is near $x = 5$ mm at $t = 5$ s. Notably, the temperature increment deceases fast within $x = 0.5 \sim 1$ mm due to the absence of plasma spots. After this region, the temperature increment decreases slightly until the later abrupt turn near $x = 22$ mm. In the case of $V_{pp} = 18$ kV, the temperature is nearly constant within $x = 1 \sim 2$ mm. As mentioned in Fig.7, this region with a very small temperature change is a result of the plasma glow and plasma streamers. The second turn appears near $x = 22$ mm in both cases, just at the edge of the insulated electrode. After this position, both of the temperature increment and its growth rate become much smaller.

Figure.9(a) and Fig.9(b) show the spanwise-averaged temporal temperature increment ΔT at $x = 3$ mm and $x = 15$ mm with different V_{pp}. For each V_{pp}, the temperature growth rate is very fast at the beginning and then decreases quickly to a low level. For instance, near the exposed electrode ($x = 3$ mm, see Fig.9(a)), the maximum temperature growth rate is $\Delta\dot{T} \approx 3°C/s$ in the case of $V_{pp} = 18$ kV. It then decreases rapidly to $\Delta\dot{T} \approx 0.5°C/s$ when $t = 20$ s and continues to decrease to $\Delta\dot{T} \approx 0.1°C/s$ at $t = 120$ s. At the downstream location of $x = 15$ mm, (see Fig.9(b)), the temperature growth rate drops from $\Delta\dot{T} \approx 0.2°C/s$ to $\Delta\dot{T} \approx 0.1°C/s$ during the first 50 seconds. Evolutions of the local temperature increment are analogous to exponential functions ($f(x) = a - b\exp(-cx)$). The temperature increments ΔT at both locations are larger with the higher applied peak-to-peak voltage. In Fig.9(c), it is obvious that the temperature increments at $t = 200$ s increase linearly with $(V_{pp})^{3.5}$. The local temperature increment is proportional to the electric power consumption too.

E. Discussion

When the AC-DBD plasma actuator is operated at the high voltage, it induces ionic wind and generates heat. More specifically, the energy consumption of the AC-DBD plasma actuator is converted into the kinetic energy of the induced flow, the thermal energy of the induced flow, and the thermal energy of the actuator itself, which can be written in the time-rate change form as

$$P_E = P_M + \dot{q}_{air} + \dot{q}_{actuator} \tag{3}$$

where P_E is the power consumption of the AC-DBD plasma actuator, P_M is the mechanical power (the kinetic energy increase rate of the induced flow), $\dot{q}_{air}$ is the heat transfer rate to the surrounding air, and $\dot{q}_{actuator}$ is the heat transfer rate to the actuator. It is known that the electromechanical efficiency of an AC-DBD plasma actuator is very low, usually less than 5%[20]. Most of the power consumption of an AC-DBD plasma actuator releases into the surrounding environment as heat due to two mechanisms: the dielectric heating mechanism and the plasma heating mechanism [24]. The dielectric heating mechanism occurs because of dielectric loss. As demonstrated in Eq.2 and Table 1, the power of dielectric heating is relatively small; thus, most of the heat comes from the plasma heating mechanism. Generally, the plasma generated by an AC-DBD plasma actuator is nonthermal plasma [16], in which heavy species have temperatures close to the ambient temperature, while the electron temperature is much higher. However, very low-value but high-frequency heating still can raise the temperature in the regions in which the plasma discharge occurs. In this study, very strong discharges are generated by the actuator along the exposed electrode, which are observed as the bright plasma streamers and plasma spots shown in Fig.2(a). Thus, the temperature distribution of the dielectric surface near the exposed electrode is irregular along the spanwise direction. The surface temperature in regions covered by the plasma streamers and plasma spots is much higher than that in the surrounding area; this temperature difference can even exceed $20^{\circ}C$, as shown in Fig.7. This confirms that the dominant thermal energy of the AC-DBD plasma actuator is generated by the plasma heating mechanism. Furthermore, the temperature of the gas-plasma mixture is not uniform in the spanwise direction, which may induce crossflow convective instability.

From the spanwise-averaged dielectric temperature, the dielectric surface can be divided into three typical regions in the streamwise direction: the plasma region ($x \in [\,0,\,5)\ mm$), the insulated electrode region ($x \in [\,5,\,22)\ mm$) and the far field region ($x \in [\,22,\,\infty)\ mm$). In the plasma region, the dielectric surface is covered by the plasma. Because the plasma is the dominant heating source, the spanwise-averaged surface temperature is much higher than that in other two regions. Because of the absence of plasma, the surface temperature in the insulated electrode region is not high. The temperature of the local dielectric increases because it generates heat due to the dielectric losses, it exchanges the thermal energy from the induced flow, and it receives thermal energy from the plasma region. Meanwhile, part of the thermal energy of the local dielectric layer is transferred to the far field region through internal thermal conduction. In the far field region, the surface temperature becomes much smaller. The local thermal energy is provided by thermal convection with the

induced flow or the ambient air, and the internal thermal conduction from the upstream regions. It should be noted that the thermal conductivity of the acrylic layer, $k \approx 0.2\ W/(m{\cdot}K)$, is extremely small. Thus, the thermal conduction inside the dielectric layer is quite slow, and the surface temperature drops considerably near the edges between regions.

Temporally, the dielectric surface temperature increases rapidly at the beginning, and then its growth rate decreases to an extremely low level. As shown in Fig.9, the evolution of the temperature increment is analogous to an exponential function, similar to evolutions of plasma emission (see Fig.2(b)). Enloe, *et al.* [14] demonstrated that the plasma emission is proportional to the current across the actuator, which suggests that the temperature increase of the dielectric layer and the surrounding air enhances the discharge phenomenon. Thus, more charged particles can be generated at a time. In Fig.2(a), it is also observed that the region covered by the plasma extends downstream during the measurement. Therefore, the accelerating distance of charged particles becomes longer, and more momentum can be added to the induced flow by the actuator. This is confirmed by the increasing velocity profile of the induced flow measured by PIV. This result is consistent with those demonstrated in previous studies [36, 37], in which the momentum induced by the AC-DBD plasma actuator increases when the dielectric layer is heated or the ambient temperature is increased.

Generally, an AC-DBD plasma actuator is interpreted as a series of sub-circuits in parallel. Each sub-circuit is a combination of the dielectric layer capacitance, the gas capacitance and the gas resistance[43, 48]. Thus, during the non-ionization period in each AC cycle, the charging in the circuit has the relationship as

$$C_a \frac{dV_a}{dt} = C_d \frac{dV_d}{dt} \tag{4}$$

where C_a is the capacitance of air, V_a is the voltage across air, C_d is the capacitance of dielectric layer, and V_d is the voltage across dielectric layer. The relationship between C_a and C_d can be drawn as

$$\frac{1}{C_a} + \frac{1}{C_d} = \frac{1}{C_{cold}} \tag{5}$$

Thus, the voltage ratio between the air and the dielectric layer during the non-ionization period, $\frac{dV_a}{dt} / \frac{dV_d}{dt}$, can be rewritten by substituting valuables with Eq.4 and Eq.5, given as

$$\frac{dV_a}{dt} / \frac{dV_d}{dt} = \frac{C_d}{C_{cold}} - 1 \tag{6}$$

During the ionization period, the air capacitance is broken down and the value of C_{eff} approximately equals to C_d. As shown in Fig.3(c), C^+_{eff} increased continuously during the experiment. Therefore, the value of the dielectric capacitor C_d also increased temporally. This is consistent with the phenomenon that the increase of temperature (before the glass transition temperature) can lead to a rapid gain of its dielectric constant[49]. Although both C^+_{eff} and C_{cold} increase simultaneously during the experiment (see Fig.3), the increment of C^+_{eff} (C_d) is much larger than the increment of C_{cold}.

Thus, the voltage ratio $\frac{dV_a}{dt}/\frac{dV_d}{dt}$ during the non-ionization period increases accordingly. As a result, V_a approached to critical voltage V_{crit} earlier when the temperature of the dielectric increases and thus the duration of the discharge process extends in each AC cycle.

Another important factor that is responsible for the enhanced discharging is the increasing temperature of gas-plasma mixture in the plasma region. Although the global gas temperature change is not significant, which can be known from the low temperature increment of the dielectric surface in the downstream of the plasma region, the gas-plasma mixture can be extremely hot at positions where discharges occur. The local density of the gas-plasma mixture decreases correspondingly. Therefore, the local reduced electric field strength (defined as E/N, where E is the electric field and N is concentration of particles) can increase greatly, resulting in a lower threshold voltage V_{crit} and a stronger discharge current. The discharge is enhanced temporally and spatially, and more particles are charged[15, 50]. Meanwhile, the mean free path of particles becomes longer due to the density decrease, leading to an increasing kinetic energy of charged particles when they collide[36, 37]. Consequently, the plasma streamers and glow regions grow to the far downstream region, and more electric power is converted into mechanical power inside the high-temperature gas-plasma mixture. Globally, the momentum flux of the induced flow increases temporally. These temperature-induced phenomena are analogous to those caused by the ambient pressure change[36, 51].

IV. Conclusion

The AC-DBD plasma actuator is a popular pneumatic method for active flow control that can induce a wall-jet-like flow on its surface. However, most of the consumed energy is released to the environment in the form of heat. It is necessary to examine the spontaneous thermal effect on the performance of the AC-DBD plasma actuator. In this study, we conducted an experimental investigation to measure the profile of the induced flow, power consumption, plasma light emission, and temperature of the dielectric layer. According to the plasma light emission and the surface temperature distribution, the dielectric surface can be divided into three typical regions in the streamwise direction: the plasma region, the insulated electrode region and the far field region. The dominant heat generation occurs in the plasma region due to the plasma discharge, where the maximum temperature increment is observed. The surface temperature is not uniform along the spanwise direction because of the irregular distribution of the plasma. Temporally, both the surface temperature and the plasma brightness increase analogously to an exponential curve. The PIV measurement shows that the velocity profile of the induced flow increases temporally; therefore, the momentum injection by the AC-DBD plasma actuator is related to the heat generation. On one side, the temperature increment of the dielectric layer affects the electric properties of the AC-DBD plasma actuator. On the other side, the temperature increment of the gas-plasma mixture benefits the local induced electric field and results in longer mean free paths of particles and stronger discharges accordingly. Consequently, the spontaneous heat generation of the AC-DBD plasma actuator enhances the induced ionic wind. The performance of the actuator is time dependent during the early period of the operation, which should be

taken into consideration in applications of AC-DBD plasma actuators. The values of capacitance, power consumption, plasma brightness and surface temperature are proportional to 3.5 power of the applied voltage. These trends can be used to predict the power consumption and dielectric temperature of the AC-DBD actuator, which can help to reduce the risk of actuator burning down.

References

[1] Jukes, T. N., Segawa, T., and Furutani, H., "Flow control on a NACA 4418 using dielectric-barrier-discharge vortex generators," *AIAA journal*, Vol. 51, No. 2, 2012, pp. 452–464. doi:10.2514/1.j051852.

[2] Lombardi, A. J., Bowles, P. O., and Corke, T. C., "Closed-Loop Dynamic Stall Control Using a Plasma Actuator," *AIAA Journal*, Vol. 51, No. 5, 2013, pp. 1130–1141. doi:10.2514/1.j051988.

[3] Chen, Z. N., Shen, L., and Wen, C. Y., "Flow Control on a Bluff Body Using Dielectric Barrier Discharge Plasma Actuators," *AIAA Journal*, 2019, pp. 2670–2674. doi:10.2514/1.J058196.

[4] Wang, L., Wong, C. W., Lu, Z., Wu, Z., and Zhou, Y., "Novel Sawtooth Dielectric Barrier Discharge Plasma Actuator for Flow Separation Control," *AIAA Journal*, Vol. 55, No. 4, 2017, pp. 1405–1416. doi:10.2514/1.j055507.

[5] Wicks, M., Thomas, F. O., Corke, T. C., Patel, M., and Cain, A. B., "Mechanism of Vorticity Generation in Plasma Streamwise Vortex Generators," *AIAA Journal*, Vol. 53, No. 11, 2015, pp. 3404–3413. doi:10.2514/1.j053997.

[6] Jukes, T. N., and Choi, K.-S., "Control of unsteady flow separation over a circular cylinder using dielectric-barrier-discharge surface plasma," *Physics of Fluids*, Vol. 21, No. 9, 2009, p. 094106. doi:10.1063/1.3237151.

[7] Thomas, F. O., Kozlov, A., and Corke, T. C., "Plasma actuators for bluff body flow control," *44th AIAA Aerospace Sciences Meeting and Exhibit*, 2006. doi:10.2514/6.2006-2845.

[8] Huang, X., and Zhang, X., "Streamwise and spanwise plasma actuators for flow-induced cavity noise control," *Physics of Fluids*, Vol. 20, No. 3, 2008, p. 037101. doi:10.1063/1.2890448.

[9] Li, Y., Zhang, X., and Huang, X., "The use of plasma actuators for bluff body broadband noise control," *Experiments in fluids*, Vol. 49, No. 2, 2010, pp. 367–377. doi:10.1007/s00348-009-0806-3.

[10] Nelson, R. C., Corke, T. C., He, C., Othman, H., Matsuno, T., Patel, M., and Ng, T. T., "Modification of the flow structure over a UAV wing for roll control," *45th AIAA Aerospace Sciences Meeting and Exhibit*, 2007. doi:10.2514/6.2007-884.

[11] Shen, L., and Wen, C.-y., "Leading edge vortex control on a delta wing with dielectric barrier discharge plasma actuators," *Applied Physics Letters*, Vol. 110, No. 25, 2017, p. 251904. doi:10.1063/1.4989901.

[12] Shen, L., Wen, C.-y., and Chen, H.-A., "Asymmetric Flow Control on a Delta Wing with Dielectric Barrier Discharge Actuators," *AIAA Journal*, Vol. 54, No. 2, 2016, pp. 652–658. doi:10.2514/1.j054373.

[13] Abbasi, A. A., Li, H., and Meng, X., "Coupled Aerodynamic and Thermal Effects for Steady and Unsteady Plasma Actuation," *AIAA Journal*, 2019, pp. 1–8. doi:10.2514/1.J058458.

[14] Enloe, C. L., McLaughlin, T. E., Van Dyken, R. D., Kachner, K. D., Jumper, E. J., and Corke, T. C., "Mechanisms and Responses of a Single Dielectric Barrier Plasma Actuator: Plasma Morphology," *AIAA Journal*, Vol. 42, No. 3, 2004A, pp. 589–594. doi:10.2514/1.2305.

[15] Brandenburg, R., "Dielectric barrier discharges: progress on plasma sources and on the understanding of regimes and single filaments," *Plasma Sources Science and Technology*, Vol. 26, No. 5, 2017, p. 053001. doi:10.1088/1361-6595/aa6426.

[16] Moreau, E., "Airflow control by non-thermal plasma actuators," *Journal of Physics D: Applied Physics*, Vol. 40, No. 3, 2007, pp. 605–636. doi:10.1088/0022-3727/40/3/s01.

[17] Corke, T. C., Enloe, C. L., and Wilkinson, S. P., "Dielectric Barrier Discharge Plasma Actuators for Flow Control," *Annual Review of Fluid Mechanics*, Vol. 42, No. 1, 2010, pp. 505–529. doi:10.1146/annurev-fluid-121108-145550.

[18] Wang, J.-J., Choi, K.-S., Feng, L.-H., Jukes, T. N., and Whalley, R. D., "Recent developments in DBD plasma flow control," *Progress in Aerospace Sciences*, Vol. 62, 2013, pp. 52–78. doi:10.1016/j.paerosci.2013.05.003.

[19] Fridman, A., Chirokov, A., and Gutsol, A., "Non-thermal atmospheric pressure discharges," *Journal of Physics D: Applied Physics*, Vol. 38, No. 2, 2005, pp. R1–R24. doi:10.1088/0022-3727/38/2/r01.

[20] Laurentie, J.-C., Jolibois, J., and Moreau, E., "Surface dielectric barrier discharge: Effect of encapsulation of the grounded electrode on the electromechanical characteristics of the plasma actuator," *Journal of Electrostatics*, Vol. 67, No. 2-3, 2009, pp. 93–98. doi:10.1016/j.elstat.2009.01.056.

[21] Aleksandrov, N., Kindysheva, S., Nudnova, M., and Starikovskiy, A. Y., "Mechanism of ultra-fast heating in a non-equilibrium weakly ionized air discharge plasma in high electric fields," *Journal of Physics D: Applied Physics*, Vol. 43, No. 25, 2010, p. 255201. doi:10.1088/0022-3727/43/25/255201.

[22] Joussot, R., Hong, D., Rabat, H., Boucinha, V., Weber-Rozenbaum, R., and Chesneau, A. L., "Thermal characterization of a dbd plasma actuator: Dielectric temperature measurements using infrared thermography," *40th AIAA Fluid Dynamics Conference and Exhibit*, 2010. doi:10.2514/6.2010-5102.

[23] Tirumala, R., Benard, N., Moreau, E., Fenot, M., Lalizel, G., and Dorignac, E., "Temperature characterization of dielectric barrier discharge actuators: influence of electrical and geometric parameters," *Journal of Physics D: Applied Physics*, Vol. 47, No. 25, 2014. doi:10.1088/0022-3727/47/25/255203.

[24] Rodrigues, F., Pascoa, J., and Trancossi, M., "Heat generation mechanisms of DBD plasma actuators," *Experimental Thermal and Fluid Science*, Vol. 90, 2018, pp. 55–65. doi:10.1016/j.expthermflusci.2017.09.005.

[25] Hu, H., Li, H., Meng, X., Wang, J., Liu, F., and Luo, S., "Starting flow by repetitive nanosecond pulsed DBD actuation at microseconds and milliseconds in quiescent air," *46th AIAA Plasmadynamics and Lasers Conference*, 2015. doi: 10.2514/6.2015-2956.

[26] Zhao, Z.-J., Cui, Y. D., Li, J.-M., Zheng, J.-G., and Khoo, B. C., "On the boundary flow using pulsed nanosecond DBD plasma actuators," *Modern Physics Letters B*, Vol. 32, No. 12n13, 2018. doi:10.1142/s0217984918400353.

[27] Zhao, Z., Li, J.-M., Zheng, J., Cui, Y. D., and Khoo, B. C., "Study of Shock and Induced Flow Dynamics by Nanosecond Dielectric-Barrier-Discharge Plasma Actuators," *AIAA Journal*, Vol. 53, No. 5, 2015, pp. 1336–1348. doi:10.2514/1.j053420.

[28] Cai, J., Tian, Y., Meng, X., Han, X., Zhang, D., and Hu, H., "An experimental study of icing control using DBD plasma actuator," *Experiments in Fluids*, Vol. 58, No. 8, 2017. doi:10.1007/s00348-017-2378-y.

[29] Liu, Y., Kolbakir, C., Hu, H., and Hu, H., "A comparison study on the thermal effects in DBD plasma actuation and electrical heating for aircraft icing mitigation," *International Journal of Heat and Mass Transfer*, Vol. 124, 2018, pp. 319–330. doi:10.1016/j.ijheatmasstransfer.2018.03.076.

[30] Pouryoussefi, S. G., Mirzaei, M., Alinejad, F., and Pouryoussefi, S. M., "Experimental investigation of separation bubble control on an iced airfoil using plasma actuator," *International Journal of Heat and Mass Transfer*, Vol. 100, 2016, pp. 1334–1341. doi:10.1016/j.applthermaleng.2016.02.133.

[31] Meng, X., Hu, H., Li, C., Abbasi, A. A., Cai, J., and Hu, H., "Mechanism study of coupled aerodynamic and thermal effects using plasma actuation for anti-icing," *Physics of Fluids*, Vol. 31, No. 3, 2019, p. 037103. doi:10.1063/1.5086884.

[32] Cheong, M., Greig, A., Gibson, B., and Arjomandi, M., "An investigation into the effect of electric field on the performance of Dielectric Barrier Discharge plasma actuators," *Experimental Thermal and Fluid Science*, Vol. 35, No. 8, 2011, pp. 1600–1607. doi:10.1016/j.expthermflusci.2011.07.011.

[33] Hasan, M. I., Morabit, Y., Dickenson, A., and Walsh, J. L., "Impact of electrode geometry on an atmospheric pressure surface barrier discharge," *Applied Physics Letters*, Vol. 110, No. 26, 2017, p. 264101. doi:10.1063/1.4985030.

[34] Mishra, B. K., and Panigrahi, P. K., "Formation and characterization of the vortices generated by a DBD plasma actuator in burst mode," *Physics of Fluids*, Vol. 29, No. 2, 2017, p. 024104. doi:10.1063/1.4975156.

[35] Zhang, L., Li, X., Che, X., Nie, W., Li, J., Zhang, Z., Chen, Q., and Zheng, Z., "Study on the influence of actuation parameter of SDBD on induced jet in low-pressure air," *Physics of Plasmas*, Vol. 24, No. 7, 2017. doi:10.1063/1.4985569.

[36] Versailles, P., Gingras-Gosselin, V., and Vo, H. D., "Impact of Pressure and Temperature on the Performance of Plasma Actuators," *AIAA Journal*, Vol. 48, No. 4, 2010, pp. 859–863. doi:10.2514/1.43852.

[37] Erfani, R., Zare-Behtash, H., and Kontis, K., "Plasma actuator: Influence of dielectric surface temperature," *Experimental Thermal and Fluid Science*, Vol. 42, 2012, pp. 258–264. doi:10.1016/j.expthermflusci.2012.04.023.

[38] Ashpis, D., Laun, M., and Griebeler, E., "Progress toward accurate measurements of power consumption of DBD plasma actuators," *50th AIAA aerospace sciences meeting including the new horizons forum and aerospace exposition*, 2012, p. 823. doi:10.2514/6.2012-823.

[39] Hanson, R. E., Houser, N. M., and Lavoie, P., "Dielectric material degradation monitoring of dielectric barrier discharge plasma actuators," *Journal of Applied Physics*, Vol. 115, No. 4, 2014, p. 043301. doi:10.1063/1.4862309.

[40] Shen, L., Chen, Z., and Wen, C., "Experimental Investigation of the Flow Structure over a Delta Wing Via Flow Visualization Methods," *Journal of visualized experiments: JoVE*, , No. 134, 2018. doi:10.3791/57244.

[41] Raffel, M., Willert, C. E., Scarano, F., Kähler, C. J., Wereley, S. T., and Kompenhans, J., *Particle image velocimetry: a practical guide*, Springer, 2018.

[42] Fridman, A., and Kennedy, L. A., *Plasma physics and engineering*, CRC Press, 2011.

[43] Kriegseis, J., Möller, B., Grundmann, S., and Tropea, C., "Capacitance and power consumption quantification of dielectric barrier discharge (DBD) plasma actuators," *Journal of Electrostatics*, Vol. 69, No. 4, 2011, pp. 302–312. doi:10.1016/j.elstat.2011.04.007.

[44] Jukes, T. N., Choi, K. S., Segawa, T., and Yoshida, H., "Jet flow induced by a surface plasma actuator," *Proceedings of the Institution of Mechanical Engineers, Part I: Journal of Systems and Control Engineering*, Vol. 222, No. 5, 2008, pp. 347–356. doi:10.1243/09596518jsce504.

[45] Kroschwitz, J. I., *Concise encyclopedia of polymer science and engineering*, Wiley NY etc., 1990.

[46] Rao, V., Ashokan, P. V., and Shridhar, M. H., "Studies of dielectric relaxation and a.c. conductivity in cellulose acetate hydrogen phthalate–poly(methyl methacrylate) blends," *Materials Science and Engineering: A*, Vol. 281, No. 1-2, 2000, pp. 213–220. doi:10.1016/s0921-5093(99)00723-6.

[47] Moralev, I., Sherbakova, V., Selivonin, I., Bityurin, V., and Ustinov, M., "Effect of the discharge constriction in DBD plasma actuator on the laminar boundary layer," *International Journal of Heat and Mass Transfer*, Vol. 116, 2018, pp. 1326–1340. doi:10.1016/j.ijheatmasstransfer.2017.09.121.

[48] Orlov, D. M., *Modelling and simulation of single dielectric barrier discharge plasma actuators*, University of Notre Dame, 2006.

[49] Thakur, V. K., Vennerberg, D., Madbouly, S. A., and Kessler, M. R., "Bio-inspired green surface functionalization of PMMA for multifunctional capacitors," *RSC Advances*, Vol. 4, No. 13, 2014, pp. 6677–6684. doi:10.1039/c3ra46592f.

[50] Haddad, A., Haddad, M., Warne, D., and Warne, D., *Advances in high voltage engineering*, IET, 2004.

[51] Benard, N., Balcon, N., and Moreau, E., "Electric wind produced by a surface dielectric barrier discharge operating in air at different pressures: aeronautical control insights," *Journal of Physics D: Applied Physics*, Vol. 41, No. 4, 2008, p. 042002. doi:10.1088/0022-3727/41/4/042002.